

Structure-aware Semantic Discrepancy and Consistency for 3D Medical Image Self-supervised Learning

Tan Pan^{1,2}, Zhaorui Tan², Kaiyu Guo^{3,2}, Dongli Xu², Weidi Xu,
Chen Jiang^{2*}, Xin Guo², Yuan Qi^{1,2,4}, Yuan Cheng^{1,2*}

¹ Artificial Intelligence Innovation and Incubation Institute, Fudan University

² Shanghai Academy of Artificial Intelligence for Science

³ The University of Queensland

⁴ Zhongshan Hospital, Fudan University

pant23@m.fudan.edu.cn, jiangchen@sais.com.cn, chengyuan@sais.com.cn

Abstract

3D medical image self-supervised learning (mSSL) holds great promise for medical analysis. Effectively supporting broader applications requires considering anatomical structure variations in location, scale, and morphology, which are crucial for capturing meaningful distinctions. However, previous mSSL methods partition images with fixed-size patches, often ignoring the structure variations. In this work, we introduce a novel perspective on 3D medical images with the goal of learning structure-aware representations. We assume that patches within the same structure share the same semantics (semantic consistency) while those from different structures exhibit distinct semantics (semantic discrepancy). Based on this assumption, we propose an mSSL framework named S^2DC , achieving Structure-aware Semantic Discrepancy and Consistency in two steps. First, S^2DC enforces distinct representations for different patches to increase semantic discrepancy by leveraging an optimal transport strategy. Second, S^2DC advances semantic consistency at the structural level based on neighborhood similarity distribution. By bridging patch-level and structure-level representations, S^2DC achieves structure-aware representations. Thoroughly evaluated across 10 datasets, 4 tasks, and 3 modalities, our proposed method consistently outperforms the state-of-the-art methods in mSSL.

1. Introduction

Self-supervised learning (SSL) is widely used in medical image analysis to build strong representations that improve performance on various applications and maximize

* Corresponding authors. This research was conducted during an internship at the Shanghai Academy of Artificial Intelligence for Science.

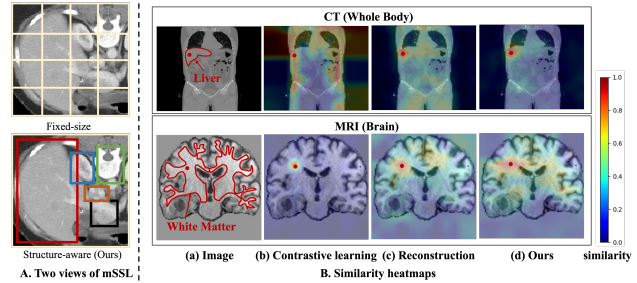


Figure 1. A. Two views of mSSL. B. Similarity heatmaps on CT and MRI images across different methods. We sample an anchor patch (red dots) and compute feature similarities with all other patches. In the first row, the liver anchor should show low similarity with non-liver patches, while in the second row, the white matter anchor should exhibit high similarity with other white matter patches. Current SOTA contrastive-based [40] (b) and reconstruction-based [39] (c) methods struggle with both patch feature discrepancy in different structures and consistency in the same structure. In contrast, our method (d) advances both discrepancy and consistency.

the use of unlabeled data [23, 39, 40]. These applications frequently focus on different specific anatomical structures (i.e., organ segmentation), each distinguished across anatomy due to location, scale, morphology, and other variations [4, 9, 10, 29]. For example, the liver is a large, well-defined solid organ with relatively homogeneous intensity and distinct anatomical boundaries. In contrast, veins are thin, tubular structures with varying diameters, lower contrast, and complex branching patterns.

Current medical image SSL (mSSL) methods can be classified into contrastive-based and reconstruction-based methods [14, 17, 39, 40]. For example, Wang et al. utilize multi-view reconstruction to encourage dense representations, while Wu et al. incorporate overlapped patch ratio

as soft contrastive constraint to improve semantic consistency. However, these methods use fixed-size image partition, treating all segmented patches uniformly across structures and overlooking their underlying semantic relationship among structures as shown in Fig. 1 A. To illustrate these limitations, we visualize similarity heatmaps on CT and MRI images across different methods by overlaying similarity scores onto the original images (Fig. 1 B). Ideally, patches within the same organ should exhibit high similarity, while those from different organs should show low similarity. However, as shown in Fig. 1 (a) and (b), existing methods struggle with maintaining intra-structure patch consistency and distinguishing inter-structure patch differences. A more detailed analysis and metrics of organ-level relationships in the state-of-the-art (SOTA) methods are provided in Fig. 5.

Based on these empirical analyses, we propose that patches within the same structure should share the same semantics, while those from different structures should exhibit distinct semantics. To achieve this, patch relationships must be structure-aware and adaptively adjusted to account for anatomical variations. Based on this assumption, we define structure-aware learning through two key principles: intra-structure consistency and inter-structure discrepancy.

To achieve these principles, we propose S^2DC , a self-supervised learning framework for 3D medical imaging designed to capture **Structure-aware Semantic Consistency** and **Discrepancy**. The core idea of our framework is to explore semantic relevance between patches to enhance structure-level representations, which unfolds in two key steps. First, we increase the discrepancy between patches with different semantics through patch-to-patch discrepancy. By an optimal transport strategy, patches with different semantics are pushed further apart. Second, beyond patch-wise distinction, the framework further explores patch-to-structure semantic consistency, leveraging the observation that patches with shared semantics form peaks in the similarity distribution. These distributional characteristics serve as soft regularization, identifying patches belonging to the same structure and enforcing structural-level consistency. Notably, the principles of inter-structure discrepancy and intra-structure consistency of our framework are also suitable for functional imaging or metabolic imaging.

The contributions of this work can be summarized as follows:

- We propose a novel insight of intra-structure consistency and inter-structure discrepancy in the anatomical structure-aware feature learning in 3D medical images. We argue that the patches within the same anatomical structures maintain consistent semantics, while the patches from different anatomical structures reflect distinct semantics.

- Based on our insight and assumption, we propose S^2DC , a novel training framework that enhances inter-structure discrepancy and intra-structure consistency. The framework establishes reliable patch-to-patch correspondences to reinforce discrepancy while leveraging patch-to-structure semantic connectivity from the similarity distribution to improve consistency.
- Our method demonstrates superior performance over SOTA medical image SSL methods, evaluated across 10 datasets, 4 tasks, and 3 imaging modalities. The code will be available upon publication.

2. Related work

SSL in 3D medical images. Contrastive-based and reconstruction-based SSL are among the most prominent paradigms in mSSL. Some approaches emphasize the fine-grained capabilities of models, incorporating techniques such as multi-scale reconstruction or reconstruction from disarranged images to enhance model performance [34, 50, 51]. Simultaneously, other methods [40, 48] prioritize preserving maximal semantic information by leveraging contextual priors. Recently, several studies have explored the combination of contrastive learning (CL) and reconstruction to further improve model performance [15, 17, 33, 39]. These works aim to learn consistent semantic representations by applying contrastive learning to global features or predicting missing information from available context. However, in mSSL, few approaches enforce constraints to enhance both anatomical structure-aware discrepancy and consistency, which is the central focus of this paper.

Geometric approaches for medical image analysis. Our method adopts some geometric characteristics for patch-to-patch correspondence. In radiographic imaging, geometric characteristics, such as location and anatomical structure, play a crucial role in organ identification, disease diagnosis, and medical analysis. Several approaches [16, 26] have incorporated consistent and recurrent anatomical patterns as learnable priors to enhance medical image analysis. For example, Huang et al. proposed to enhance segmentation by establishing patch correspondence between two 2D images. Those methods utilizing the geometric or anatomical invariant have shown remarkable improvement in the downstream tasks. Some medical SSL works [15, 20] also explore geometric correspondence for better performance. The SSL method GVSL [15] considers the geometric transformation and reconstructs affined images to original images to learn global and local representations. Yang et al. present a keypoint-augmented fusion layer with the keypoint guidance from SIFT to extract local and global information to improve segmentation results. Those methods leverage the invariance of anatomical structures while not considering the relation between anatomical structures.

Multi-scale features in SSL. Multi-scale features have

received much attention in existing SSL research, which is relevant but not sufficient to structure-aware representations. Multi-scale feature learning in SSL can be categorized as reconstruction-based and contrastive-based methods. For instance, the contrastive-based method [Wang et al.](#) introduced a dense constraint based on the correspondence of local features for dense prediction tasks. The method [\[37\]](#) developed data-driven contrastive learning methods by utilizing prototypes. [Zhou et al.](#) combines multi-scale reconstruction and multi-scale contrastive learning to learn multi-scale features. Although those methods achieve success in learning multi-scale features, they are not aware of anatomical structure variations because of the fixed-size image partition strategy and uniform contribution of different anatomical structures in images.

3. Methods

We present our two-step approach: patch-to-patch discrepancy and patch-to-structure consistency. The patch-to-patch constraint increases the distance between all patches, ensuring that patches with different semantics are pushed further apart. In contrast, the patch-to-structure constraint keeps patches within the same structure close together, enforcing semantic consistency within the same structure.

3.1. Preliminaries

Contrastive Learning. Contrastive learning in SSL constructs positive sample pairs to capture shared information [\[23, 36\]](#), typically using a source image and its augmented counterpart as two views of the same image. Based on the theory that the features learned from these paired views suffice for downstream tasks [\[36\]](#), we focus solely on positive pairs from the same source image rather than different ones. We adopt vanilla InfoNCE in MoCo [\[13\]](#) as our baseline, leveraging a teacher-student mechanism and a queue storing previously generated features. Following prior SSL methods in 3D medical imaging, images are partitioned into multiple sub-volumes to optimize memory efficiency [\[14, 39, 40\]](#). Given N non-overlapping subvolumes $\{v_k | k = 1, 2, 3, \dots, N\}$ cropped from a full volume \mathcal{V} , we randomly select a subvolume v_i and generate an augmented version v'_i as a positive pair. The constraint follows a dictionary look-up strategy, where a query feature is matched against candidate features in the dictionary. More details can be found in Appendix.

Based on the dictionary $\{q_m^* | m = 1, 2, \dots, K\}$ where q_m^* is the feature encoded by the teacher model and K is the size of the dictionary and the query q_i encoded by the student model, the InfoNCE loss is conducted as a contrastive loss \mathcal{L}_g :

$$\mathcal{L}_g = -\log \frac{\exp \left(q_i \cdot q_i^* / \tau \right)}{\sum_{m=0}^K \exp (q_i \cdot q_m^*) / \tau}, \quad (1)$$

where τ is a temperature hyper-parameter [\[13\]](#).

Geometric equivariance. [Mao et al.](#) [\[21\]](#) propose that the model satisfies equivariance, a meta-property that can be applied to dense feature maps and generalized to most existing vision tasks. Equivariance implies that geometric transformations applied to the input image are preserved in the output features, which benefits many tasks [\[3, 21\]](#). Consequently, we expect the token features from the Transformer encoder φ to undergo the same homography transformation as the input images. Based on this assumption, we can establish correspondences between token features in the two input volumes to compute patch-to-patch and patch-to-structure relationships. Remarkably, we consider each token to correspond to a patch in the input volume.

3.2. Patch-to-patch discrepancy

Given a volume \mathcal{V}_i and its augmented counterpart \mathcal{V}'_i , we build patch-to-patch correspondence between them. A reliable patch-to-patch correspondence refers to correct one-to-one alignment among two patch sets, which treats every patch as a distinct object. This step aims to enlarge the distribution gap between all semantics and capture distinct characteristics.

In mSSL, augmentations can be broadly classified into geometric and intensity transformations, with only geometric transformations affecting voxel positions. Geometric transformations involve modeling an affine matrix H , which is applied to the target image to alter its spatial configuration. Therefore, in this section, we discuss the situation after applying an affine transformation.

Ground truth of patch correspondence. Given two patch centers $c_i = (x_i, y_i, z_i)$ and $c_j = (x_j, y_j, z_j)$ from \mathcal{V}_i and \mathcal{V}'_i , where x , y , and z are coordinates, the correspondence between two patches is determined based on the re-projection distance of their central positions mapped in the input volume, as described in Eq. (2) and Eq. (3).

$$\mathcal{M}_{gt}(i, j) \triangleq \begin{cases} 1 & \text{if } \langle H(c_i), c_j \rangle \wedge \langle H^{-1}(c_j), c_i \rangle, \\ 0 & \text{else.} \end{cases} \quad (2)$$

Here, $H^{-1}(\cdot)$ denotes the inverse of the affine transformation $H(\cdot)$ in 3D space, yielding the transformed position. The notation $\langle \cdot, \cdot \rangle$ serves as the metric to determine whether two patches originate from the same patch. Specifically, the metric is:

$$\langle H(c_i), c_j \rangle \triangleq \begin{cases} 1, \text{if } (\Delta x_{ij}, \Delta y_{ij}, \Delta z_{ij}) \\ \in [-\frac{W}{2}, \frac{W}{2}] \times [-\frac{H}{2}, \frac{H}{2}] \times [-\frac{D}{2}, \frac{D}{2}], \\ 0, \text{else,} \end{cases} \quad (3)$$

Here, W , H and D are the width, height and depth of patch and Δx_{ij} , Δy_{ij} and Δz_{ij} are the coordinate differences of

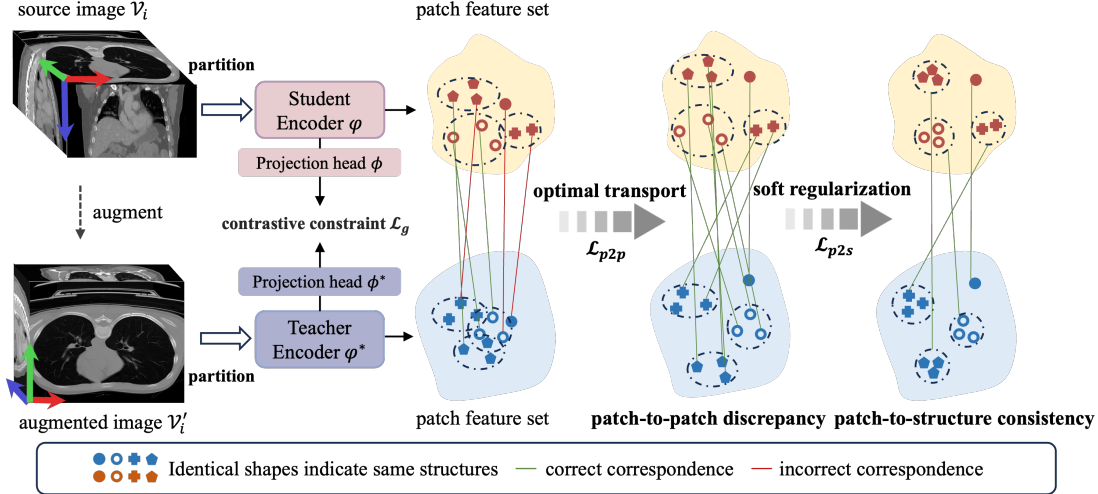


Figure 2. The pipeline of our SSL framework. S^2DC is established on patch features (i.e., token feature in vision transformer) and incorporates two main steps: (1) Patch-to-patch discrepancy. The model aligns two patch sets, which treats every patch as distinct semantics to enlarge the distribution gap between all semantics. (2) Patch-to-structure consistency. The model applies a soft regularization to align patches within the same structure. By those two steps, the framework captures semantic connectivity between anatomical structures.

$H(c_i)$ and c_j . With Eq. (2) and Eq. (3), the ground-truth patch-to-patch correspondences \mathcal{M}_{gt} between two images are obtained.

Building reliable patch-to-patch correspondences.

Given token features from $\varphi^*(\mathcal{V}_i)$ and $\varphi(\mathcal{V}_i)$, we can calculate the similarity map \mathcal{M}_t between tokens and get the loss between \mathcal{M}_t and \mathcal{M}_{gt} . However, similar to the issues in image matching [27, 31], reliably identifying patch correspondence in medical images is challenging due to repetitive patterns. This intractable challenge would be optimized by solving a differentiable optimal transport problem, such as the Sinkhorn algorithm [30]. The Sinkhorn algorithm is used to solve entropy-regularized optimal transport, enabling soft assignment of correspondences between feature points by iteratively refining a doubly stochastic matrix, improving robustness to noise and deformations. The efficiency of Sinkhorn is affected by the large number of iterations.

Rocco et al. propose using a dual-softmax operator to establish reliable correspondences based on neighborhood consensus, which brings mutual nearest neighbors closer to learn a more compact similarity distribution. Given the similarity map \mathcal{M}_t between two images, the similarities after applying the dual-softmax operator is:

$$\hat{\mathcal{M}}_t(i, j) = \text{softmax}(\mathcal{M}_t(i, :)) \cdot \text{softmax}((\mathcal{M}_t(:, j))). \quad (4)$$

Based on the ground-truth correspondences \mathcal{M}_{gt} and the re-assigned feature similarity matrix $\hat{\mathcal{M}}_t$, we use the cross-entropy loss to minimize Kullback-Leibler divergence (KL divergence) between them [35]. This patch-to-patch loss

\mathcal{L}_{p2p} is:

$$\mathcal{L}_{p2p} = -\frac{1}{|\mathcal{M}_{gt}|} \sum_{i=0}^N \sum_{j=0}^N \mathcal{M}_{gt}(i, j) \times \log(\hat{\mathcal{M}}_t(i, j)), \quad (5)$$

where N represents the number of patches (i.e., tokens in the 3D Transformer).

3.3. Patch-to-structure consistency

The correspondence assignment focuses on enhancing reliable patch-to-patch correspondence, which treats every patch as distinct. Patch-to-patch discrepancy limits the exploration of connectivity among patches from the same semantics (i.e., same anatomical structure). Thus, a patch-to-structure correspondence should be explored to improve consistency.

We define neighborhood similarity distribution as \mathcal{D}_n , which represents the similarity vector of an anchor patch feature t_n from \mathcal{V}_i with all the patch features from \mathcal{V}'_i . As shown in Fig. 3, patch pairs with the same semantics form distinct peaks in the distribution \mathcal{D}_n , which meets the assumption that the same structures have the same semantics. Thus, the central tendency and dispersion of \mathcal{D}_n can be employed to constrain semantic connectivity. For instance, if t_n is similar to several patches of \mathcal{V}'_i , indicating they may belong to the same anatomical structure, \mathcal{D}_n tends to be more dispersed (Fig. 3 (b)). In contrast, with no semantic-similar patches, the distribution of t_n is more concentrated. Therefore, we utilize the characteristics of \mathcal{D}_n as a soft label to regularize the patch-to-patch loss \mathcal{L}_{p2p} to maintain underlying semantic relevance.

We introduce a simplified version of the Sharpe ratio [28] to reflect the dispersion and concentration of neighborhood

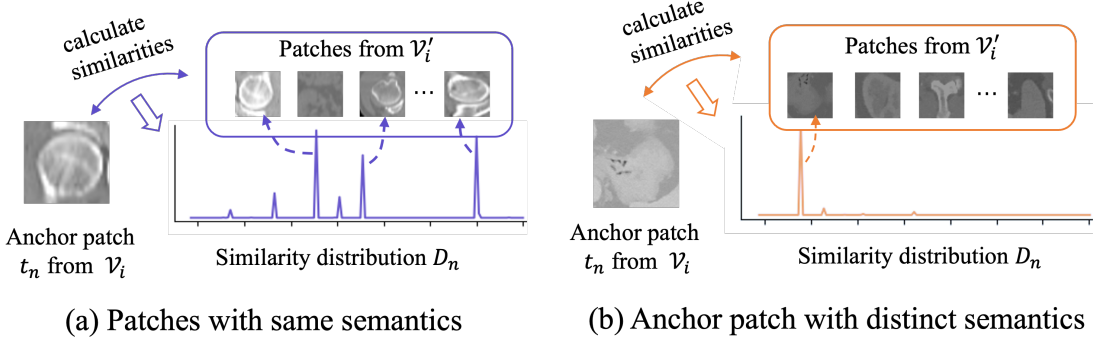


Figure 3. Illustration of the similarity distribution D_n . (a) Patches with the same semantics (e.g., bone). Given an anchor patch, patches from the same semantics form several peaks in D_n . (b) Anchor patch with distinct semantics (e.g., pancreas), D_n shows only one large peak (its augmented patch).

similarity distribution D_n . Given the D_n of the patch feature t_n , the Sharpe ratio of t_n can be computed as:

$$sr_{V_i}^n = \frac{\max(D_n) - \frac{1}{N} \sum_{m=1}^N D_n}{\sigma_{D_n}}, \quad (6)$$

where, σ_{D_n} is the variance of vector D_n and the notation $\max(D_n)$ is the maximal value of D_n . A low Sharpe ratio of D_n indicates that the distribution is more dispersed, which means the patch feature t_n has more than one similar semantic patch feature. More details can be seen in Appendix.

$sr_{V_i}^n$ is utilized as the soft regularization to adaptively adjust \mathcal{L}_{p2p} , serving as soft evidence for maintaining a semantic connectivity relationship among patch features. The weighted losses for the feature t_n of the volume V_i is $\mathcal{L}_c(n, \cdot) = \text{softmax}(sr_{V_i})_n \mathcal{L}_{p2p}(n, \cdot)$, where $sr_{V_i} = \{sr_{V_i}^n\}_n$. Similarly, we have $\mathcal{L}_c(\cdot, m) = \text{softmax}(sr_{V'_i})_m \mathcal{L}_{p2p}(\cdot, m)$. Thus, we have the loss of a single pair:

$$l_{n,m} = \frac{(\text{softmax}(sr_{V_i})_n + \text{softmax}(sr_{V'_i})_m) \mathcal{L}_{p2p}(n, m)}{2}. \quad (7)$$

Finally, the patch-to-structure loss \mathcal{L}_{p2s} is

$$\mathcal{L}_{p2s} = \frac{\sum_{m=0}^N \sum_{n=0}^N l_{n,m}}{N \times N}. \quad (8)$$

3.4. Overall loss function

The final combined objective for the proposed framework is defined as:

$$\mathcal{L} = \mathcal{L}_g + \mathcal{L}_{p2p} + \mathcal{L}_{p2s}, \quad (9)$$

4. Experiments

This section begins with an overview of the datasets utilized for both pre-training and downstream tasks. Next, we provide a brief summary of the implementation details for the

method. Lastly, we present a comprehensive comparison of the experimental results for our proposed method against other SOTA SSL approaches in 3D medical imaging.

4.1. Datasets and implementation details

Pre-training and downstream datasets. Although we emphasize the anatomical structure-specific semantic connectivity, the training process of our mining semantic connective strategy is also suitable for positron emission tomography (PET). In our experiments, we include computed tomography (CT), magnetic resonance imaging (MRI), and PET modalities.

We use the same dataset settings as VoCo [40] on CT, *i.e.*, 10k data collection. BTCV and TCIA COVID-19 are used as pre-training datasets (1k data) for the BTCV segmentation task, while all other CT segmentation tasks are pre-trained on 10k data. Additionally, we collect 6605 (6k) unlabeled MRI scans from OASIS3 [18] and 3519 (3k) PET scans from UDPET [4] and ADNI [22] for pre-training. We evaluate methods on 10 datasets in 3 modalities, as shown in Tab. 2. More details about dataset splits are provided in Appendix.

Training setup. For pre-training stage, S^2DC adopts Swin-B [11] as the default backbones in three modalities, following previous works [11, 39, 40]. We set 100k iterations for pre-training in all modalities and crop subvolumes with size $96 \times 96 \times 96$. In our patch-to-patch loss \mathcal{L}_{p2p} , we adopt the dual-softmax operator for efficiency, while the results of the Sinkhorn algorithm can be found in Appendix. For downstream tasks, we adopt Swin-B and its derivative architectures. The weights of models are initialized by the weights of pre-training models. We adopt the Swin-UNETR [14] framework in segmentation, image-to-image translation, and reconstruction tasks. Swin-B [11] is used as the backbone of classification tasks. More details about pre-training and training settings can be found in Appendix.

Method	Dice Score(%)													
	Spl	RKid	LKid	Gall	Eso	Liv	Sto	Aor	IVC	Veins	Pan	RAG	LAG	AVG
From Scratch														
UNETR [12]	93.02	94.13	94.12	66.99	70.87	96.11	77.27	89.22	82.1	70.16	76.65	65.32	59.21	79.82
Swin-UNETR [14]	94.06	93.54	93.8	65.61	74.6	97.09	75.94	91.8	82.36	73.63	75.19	68	61.11	80.53
With General SSL														
MAE3D [7]	93.98	94.37	94.18	69.86	74.64	96.66	80.4	90.3	83.13	72.65	77.11	67.34	60.54	81.33
SimCLR [6]	92.79	93.04	91.41	49.65	50.99	98.49	77.92	85.56	80.58	64.37	67.16	59.04	48.99	73.85
SimMIM [41]	95.56	95.82	94.14	52.06	53.52	98.98	80.25	88.11	82.98	66.49	69.16	60.88	50.45	76.03
MoCo v3 [13]	91.96	92.85	92.42	68.25	72.77	94.91	78.82	88.21	81.59	71.15	75.76	66.48	58.81	79.54
Jigsaw [5]	94.62	93.41	93.55	75.63	73.21	95.71	80.8	89.41	84.78	71.02	79.57	65.68	60.22	81.35
PositionLabel [46]	94.35	93.15	93.21	75.39	73.24	95.76	80.69	88.8	84.04	71.18	79.02	65.11	60.07	81.09
With medical image SSL														
MG [49]	91.99	93.52	91.81	65.11	76.41	95.98	86.88	89.29	83.59	71.79	81.62	67.97	63.18	81.45
ROT [32]	91.75	93.13	91.62	65.09	<u>76.55</u>	94.21	<u>86.16</u>	89.74	83.08	71.13	81.55	67.9	63.72	81.20
Vicregl [1]	90.32	94.15	91.3	65.12	75.41	94.76	86.00	89.13	82.54	71.26	81.01	67.66	63.08	80.89
Rubik++ [34]	96.21	90.41	89.33	75.22	72.64	97.44	79.25	89.65	83.76	74.74	78.35	67.14	61.97	81.38
PCRLv1 [47]	95.73	89.66	88.53	<u>75.41</u>	72.33	96.20	78.99	89.11	83.06	74.47	77.88	67.02	61.85	80.78
PCRLv2 [48]	95.50	91.43	89.52	76.15	73.54	97.28	79.64	90.16	84.17	75.20	78.71	68.74	62.93	81.74
Swin-UNETR [14]	95.25	93.16	92.97	63.62	73.96	96.21	79.32	89.98	83.19	<u>76.11</u>	<u>82.25</u>	68.99	65.11	81.54
SwinMM [39]	94.33	94.18	94.16	72.97	74.75	96.37	83.23	89.56	82.91	70.65	75.52	69.17	62.90	81.81
GL-MAE [51]	94.54	94.39	94.37	73.19	74.93	96.51	83.49	89.74	83.11	70.80	75.71	69.39	63.12	82.01
GVSL [15]	95.27	91.22	92.25	72.69	73.56	96.44	82.40	88.90	84.22	70.84	76.42	67.48	63.25	81.87
VoCo [40]	95.73	96.53	<u>94.48</u>	76.02	75.60	<u>97.41</u>	78.43	91.21	<u>86.12</u>	78.19	80.88	<u>71.47</u>	<u>67.88</u>	<u>83.85</u>
S^2DC	96.24	96.51	94.52	74.27	77.69	96.95	83.33	90.44	86.66	75.22	84.24	68.22	69.73	84.14

Table 1. Results on the segmentation task BTCV fine-tuning from pre-training models trained on 1k CT data. Most of the results are drawn from [40, 44]. **Best** and second best are highlighted

Task	Dataset	Modality
Segmentation	BTCV [19]	CT
	MSD-Liver [29]	CT
	MSD-Lung [29]	CT
	MSD-Spleen [29]	CT
	BraTs 21 [29]	MRI
Classification	AUTOPET [10]	PET
	CC-CCII [45]	CT
Reconstruction	ADNI-cls [22]	PET
	UDPET [4]	PET
I2I translation	BraTs 23 [29]	MRI

Table 2. The downstream tasks and modalities. I2I translation represents image-to-image translation.

Comparison methods. We compare S^2DC with SOTA SSL methods in general [5–7, 13, 41, 46] and medical [1, 14, 15, 32, 34, 39, 40, 47–49, 51] images. Meanwhile, we report results of training from scratch (i.e., without initialized weights of pre-training models).

4.2. Results on downstream tasks.

We report the results of 4 downstream tasks on 3 modalities. Following previous work, we use the metrics Dice score for segmentation, accuracy for classification, PSNR, SSIM, and NMSE for I2I translation, and SSIM and PSNR for reconstruction.

Segmentation tasks. Compared to volume-level and voxel-level methods, S^2DC performs well both in small

targets (AUTOPET, MSD-Lung) and large organs (BTCV, MSD-Liver, MSD-Spleen and BraTs 21) segmentation, as shown in Tab. 1 and Tab. 3. In BTCV datasets, compared to general SSL methods, medical SSL methods show superior performance. Notably, with S^2DC pre-training, we achieve an average improvement of 4.32%, reaching a Dice score of 75.47%, which surpasses other SOTA medical SSL methods by 0.81%.

Classification tasks. We conduct experiments on the CC-CCII dataset for COVID-19 classification and ADNI for AD (Alzheimer’s Disease), MCI (Mild Cognitive Impairment), and CN (Cognitively Normal) classification. With the pre-trained model, S^2DC achieves an average improvement of 3.93% and outperforms other medical SSL methods.

Method	Network	CC-CCII	ADNI-cls	AVG
		Acc(%)	Acc(%)	Acc(%)
From Scratch				
Swin-UNETR [14]	Swin-B	88.04	56.17	72.10
With 3D medical image SSL				
PCRLv2 [48]	Swin-B	93.07	56.05	74.56
Swin-UNETR [14]	Swin-B	94.15	55.95	75.05
SwinMM [39]	Swin-B	<u>94.80</u>	<u>56.36</u>	<u>75.58</u>
VoCo [40]	Swin-B	94.60	56.32	75.46
S^2DC	Swin-B	95.34	56.72	76.03

Table 4. Experimental results on the classification task CC-CCII and ADNI-cls fine-tuning from pre-training models trained on 6k MRI scans. **Best** and second best are highlighted.

Method	Dice(%)								Total
	MSD Liver	MSD Lung	MSD Spleen	AUTOPET	BraTs21				
From scratch								WT	TC
WT	TC	ET	AVG	AVG					
Swin-UNETR [14]									
81.18	59.73	94.20	34.49	92.89	88.28	77.34	86.17	71.15	
With 3D medical image SSL									
Swin-UNETR [14]	81.58	62.46	94.49	43.85	92.70	88.42	78.82	86.64	73.95
Swin-MM [39]	82.32	61.16	94.60	44.37	92.89	<u>88.54</u>	<u>79.18</u>	<u>86.87</u>	73.86
PCRLv2 [48]	82.12	62.39	95.23	42.64	92.81	88.49	78.74	86.68	73.81
VoCo [40]	<u>82.50</u>	<u>63.34</u>	<u>95.70</u>	<u>45.10</u>	92.90	88.44	78.62	86.65	<u>74.66</u>
<i>S²DC</i>	83.43	64.40	95.73	46.47	92.76	88.71	79.79	87.09	75.47

Table 3. Results on the segmentation tasks MSD-Liver, MSD-Lung, MSD-Spleen, AUTOPET, and BraTs21. WT, TC, and ET represent the whole tumor, tumor core, and enhancing tumor, respectively. We retrained all methods using 10k, 6k, and 3k data in three modalities separately, except for VoCo in CT, whose weight is provided in the official code. **Best** and second best are highlighted.

Method	T1->T2			T1->T1ce		
	PSNR↑	NMSE↓	SSIM↑	PSNR↑	NMSE↓	SSIM↑
From Scratch						
Swin-UNETR [14]	26.57	0.1348	0.8807	26.91	0.082	0.8871
With 3D medical image SSL						
PCRLv2 [48]	26.79	0.1640	<u>0.8828</u>	29.62	0.123	0.9179
Swin-UNETR [14]	24.81	0.2938	0.8441	30.42	0.108	0.9117
SwinMM [39]	24.05	0.3158	0.8182	30.70	0.099	0.9059
VoCo [40]	25.81	0.1916	0.8598	<u>31.92</u>	<u>0.079</u>	0.9315
<i>S²DC</i>	25.96	0.1161	0.8839	32.65	0.041	0.9412

Table 5. Experimental results on the image-to-image translation task BraTs23 fine-tuning from pre-training models trained on 6k MRI scans. **Best** and second best are highlighted.

Method	Network	SSIM↑	PSNR↑
From Scratch			
Swin-UNETR [14]	-	0.99917	<u>58.4100</u>
With 3D medical image SSL			
PCRLv2 [48]	Swin-UNETR	0.99916	58.2865
Swin-UNETR [14]	Swin-UNETR	0.99917	58.3409
SwinMM [39]	Swin-UNETR	0.99917	58.4002
VoCo [40]	Swin-UNETR	0.99916	58.2561
<i>S²DC</i>	Swin-UNETR	0.99917	58.4649

Table 6. Experimental results on low-dose to full-dose reconstruction task UDPET fine-tuning from pre-training models trained on 3k PET scans. **Best** and second best are highlighted.

Image-to-image translation task. We evaluate in BraTs23, which includes four structural MRI modalities for each individual. The translation quality for T1 → T2 and T1 → T1ce are compared by peak signal-to-noise ratio (PSNR), normalized mean squared error (NMSE), and structural similarity index (SSIM) [43]. From Table 5, our method excels in two tasks. Remarkably, with *S²DC* pre-training, we gain 5.41% and 0.32% improvements in SSIM separately. We notice that other methods fail to get improvement in the task T1 → T2 compared to From Scratch. That may be due to the deep domain gap between the two sequences, while pre-trained models provide biased initializations. In contrast, *S²DC* achieves improvement in NMSE and SSIM, showing better ability in this task.

Reconstruction task. We evaluate the capabilities of reconstruction in different methods on the UDPET dataset. Following the previous work [8], whole-body data at

DFR=50 (*i.e.*, 1/50 doses) were selected to explore the reconstruction ability of all methods. This task has been extensively studied, yet our method, *S²DC*, still achieves superior PSNR results.

Overall comparisons on 10 downstream datasets.

The results demonstrate that *S²DC* performs effectively across 10 datasets and 4 tasks. Compared to training from scratch, which achieves an average score of 77.93%, *S²DC* pre-training delivers a 3.5% improvement, reaching 81.43%. Additionally, *S²DC* outperforms the second-best SSL method (VoCo [40], average score 80.65%) for all tasks, with an average gain of 0.78%. These findings indicate that *S²DC* is both reliable and adaptable across various downstream tasks and modalities.

4.3. Ablation study

Influence of different constraints. We use contrastive learning loss \mathcal{L}_g in Sec. 3.1 as our baseline. The impact of different constraints in pre-training is presented in Tab. 7. The results indicate that combining patch-to-patch loss \mathcal{L}_{p2p} and patch-to-structure loss \mathcal{L}_{p2s} yields SOTA performance compared to Tab. 1. Meanwhile, we visualize the t-SNE clustering results of 13 organs under different constraints, as shown in Fig. 4. The \mathcal{L}_{p2p} constraint leads to a sparser inter-structure distribution, while the \mathcal{L}_{p2s} constraint results in more compact intra-structure clusters. Combining \mathcal{L}_{p2p} and \mathcal{L}_{p2s} achieves the best overall clustering performance.

Baseline(\mathcal{L}_g)	BCV			AUTOPET
	$+\mathcal{L}_{p2p}$	$+\mathcal{L}_{p2s}$	DICE(%)	
•			83.43	45.72
•	•		83.98	45.85
•		•	84.02	46.23
•	•	•	84.14	46.47

Table 7. The ablation results of different constraints.

Intra-structure consistency and inter-structure discrepancy. We visualize the t-SNE of features extracted by four medical pre-trained models and calculate their silhouette

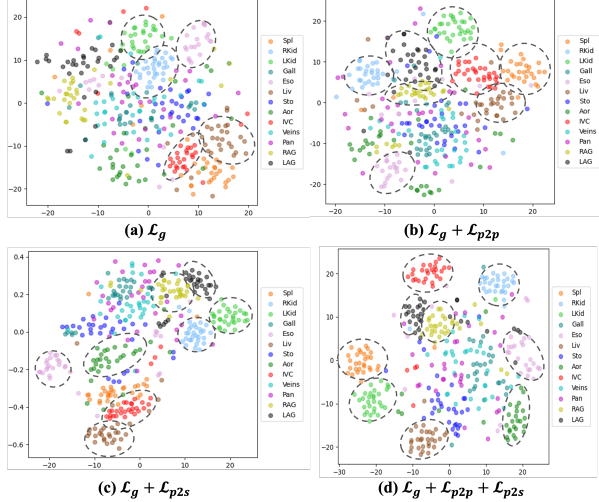


Figure 4. The t-SNE feature visualization of different losses on 13 organs on the BTCV dataset.

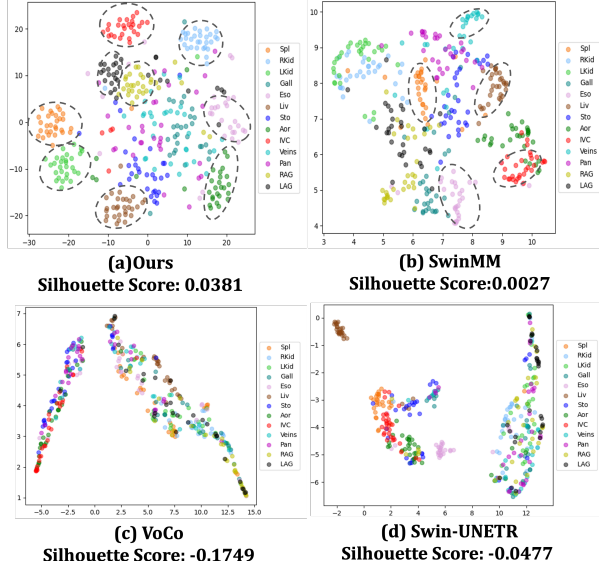


Figure 5. The t-SNE visualization of features from 13 organs on the BTCV dataset and the silhouette scores of four methods.

scores [25], which evaluate the quality of clustering by measuring how similar a data point is to its cluster (consistency) compared to other clusters (discrepancy). Fig. 5 shows the clustering capabilities of 13 organs on the BTCV dataset. S^2DC shows excellent performance on organ discrimination and consistency, which gets the highest silhouette scores. As shown in Tab. 1, most organs that cluster well also exhibit strong segmentation performance, highlighting the importance of structure-specific consistency and discrepancy. Additionally, we visualize the feature maps of 4 SSL models on 3 modalities in Fig. 6. S^2DC performs semantic consistency in the background, tissues (CT), func-

tional regions (MRI), and metabolic regions (PET).

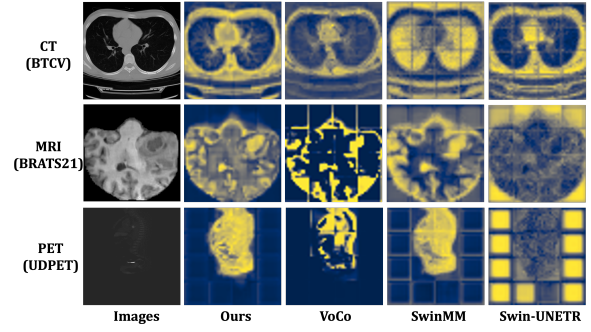


Figure 6. We visualize the first principal components after applying PCA to token features [2] within volumes of CT, MRI, and PET. The figure displays the central slices of feature maps.

Method	Accuracy(%)		
	10%	50%	100%
Swin-UNETR [14]	77.15	92.28	94.15
SwinMM [39]	87.87	93.50	94.80
VoCo [40]	86.73	92.43	94.60
S^2DC	88.29	93.89	95.34

Table 8. Experiment results on CC-CCII with various ratios of the training data. 10%, 50%, and 100% represent ratios. **Best** results are highlighted.

Varying ratios of the training dataset. We evaluate the performances of models that were trained with varying ratios of CC-CCII. From Tab. 8, S^2DC outperforms other methods under different ratios of training data. Notably, S^2DC achieves 88.29% accuracy using only 10% of the data, which is effective with limited dataset sizes.

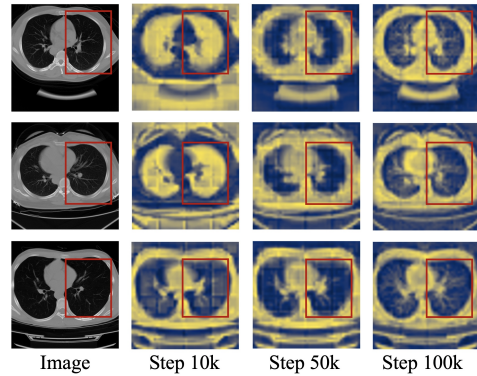


Figure 7. The evolution of patch-to-structure correspondences throughout training.

Patch-to-structure correspondences evolution. We visualize the trend of feature maps at different training steps. As shown in Fig. 7, feature consistency improves as the training progresses. Additionally, larger structures (e.g., the heart) are learned more easily than smaller ones like bronchioles, highlighting the challenge of learning small structures.

5. Conclusion

We propose S^2DC , a medical image SSL framework that enhances structure-aware semantic consistency and discrepancy by patch-to-patch and patch-to-structure steps. Experimental results and visualizations demonstrate S^2DC 's superior performance. Future exploration could include larger pre-training datasets or model generalization across modalities to support broader applications.

6. Acknowledgments

This paper was supported by the National Natural Science Foundation of China (Grant No.82394432 and 92249302), the Shanghai Municipal Science and Technology Major Project (Grant No.2023SHZDZX02). The computations in this research were performed using the CFFF platform of Fudan University.

References

- [1] Adrien Bardes, Jean Ponce, and Yann LeCun. Vicregl: Self-supervised learning of local visual features. *Advances in Neural Information Processing Systems*, 35:8799–8810, 2022. 6
- [2] Mathilde Caron, Hugo Touvron, Ishan Misra, Hervé Jégou, Julien Mairal, Piotr Bojanowski, and Armand Joulin. Emerging properties in self-supervised vision transformers. In *Proceedings of the IEEE/CVF international conference on computer vision*, pages 9650–9660, 2021. 8
- [3] Anadi Chaman and Ivan Dokmanic. Truly shift-invariant convolutional neural networks. In *Proceedings of the IEEE/CVF Conference on Computer Vision and Pattern Recognition*, pages 3773–3783, 2021. 3
- [4] Gaoyu Chen, Sheng Liu, Wenxiang Ding, Li Lv, Chen Zhao, Fenghua Weng, Yong Long, Yunlong Zan, and Qiu Huang. A total-body ultra-low dose pet reconstruction method via image space shuffle u-net and body sampling. *IEEE Transactions on Radiation and Plasma Medical Sciences*, 2023. 1, 5, 6
- [5] Pengguang Chen, Shu Liu, and Jiaya Jia. Jigsaw clustering for unsupervised visual representation learning. In *Proceedings of the IEEE/CVF conference on computer vision and pattern recognition*, pages 11526–11535, 2021. 6
- [6] Ting Chen, Simon Kornblith, Mohammad Norouzi, and Geoffrey Hinton. A simple framework for contrastive learning of visual representations. In *International conference on machine learning*, pages 1597–1607. PMLR, 2020. 6
- [7] Zekai Chen, Devansh Agarwal, Kshitij Aggarwal, Wiem Safta, Mariann Micsinai Balan, and Kevin Brown. Masked image modeling advances 3d medical image analysis. In *Proceedings of the IEEE/CVF Winter Conference on Applications of Computer Vision*, pages 1970–1980, 2023. 6
- [8] Jiaqi Cui, Pinxian Zeng, Xinyi Zeng, Yuanyuan Xu, Peng Wang, Jiliu Zhou, Yan Wang, and Dinggang Shen. Prior knowledge-guided triple-domain transformer-gan for direct pet reconstruction from low-count sinograms. *IEEE Transactions on Medical Imaging*, 2024. 7
- [9] Tugba Akinci D’Antonoli, Lucas K Berger, Ashraya K Indrakanti, Nathan Vishwanathan, Jakob Weiß, Matthias Jung, Zeynep Berkarda, Alexander Rau, Marco Reisert, Thomas Küstner, et al. Totalsegmentator mri: Sequence-independent segmentation of 59 anatomical structures in mr images. *arXiv preprint arXiv:2405.19492*, 2024. 1
- [10] Sergios Gatidis, Marcel Früh, Matthias Fabritius, Sijing Gu, Konstantin Nikolaou, Christian La Fougère, Jin Ye, Junjun He, Yige Peng, Lei Bi, et al. The autopet challenge: towards fully automated lesion segmentation in oncologic pet/ct imaging. 2023. 1, 6
- [11] Ali Hatamizadeh, Vishwesh Nath, Yucheng Tang, Dong Yang, Holger R Roth, and Daguang Xu. Swin unetr: Swin transformers for semantic segmentation of brain tumors in mri images. In *International MICCAI brainlesion workshop*, pages 272–284. Springer, 2021. 5
- [12] Ali Hatamizadeh, Yucheng Tang, Vishwesh Nath, Dong Yang, Andriy Myronenko, Bennett Landman, Holger R Roth, and Daguang Xu. Unetr: Transformers for 3d medical image segmentation. In *Proceedings of the IEEE/CVF winter conference on applications of computer vision*, pages 574–584, 2022. 6
- [13] Kaiming He, Haoqi Fan, Yuxin Wu, Saining Xie, and Ross Girshick. Momentum contrast for unsupervised visual representation learning. In *Proceedings of the IEEE/CVF conference on computer vision and pattern recognition*, pages 9729–9738, 2020. 3, 6
- [14] Yufan He, Vishwesh Nath, Dong Yang, Yucheng Tang, Andriy Myronenko, and Daguang Xu. Swinunetr-v2: Stronger swin transformers with stagewise convolutions for 3d medical image segmentation. In *International Conference on Medical Image Computing and Computer-Assisted Intervention*, pages 416–426. Springer, 2023. 1, 3, 5, 6, 7, 8
- [15] Yuting He, Guanyu Yang, Rongjun Ge, Yang Chen, Jean-Louis Coatrieux, Boyu Wang, and Shuo Li. Geometric visual similarity learning in 3d medical image self-supervised pre-training. In *Proceedings of the IEEE/CVF Conference on Computer Vision and Pattern Recognition*, pages 9538–9547, 2023. 2, 6
- [16] Junjia Huang, Haofeng Li, Guanbin Li, and Xiang Wan. Attentive symmetric autoencoder for brain mri segmentation. In *International Conference on Medical Image Computing and Computer-Assisted Intervention*, pages 203–213. Springer, 2022. 2
- [17] Yankai Jiang, Mingze Sun, Heng Guo, Xiaoyu Bai, Ke Yan, Le Lu, and Minfeng Xu. Anatomical invariance modeling and semantic alignment for self-supervised learning in 3d medical image analysis. In *Proceedings of the IEEE/CVF International Conference on Computer Vision*, pages 15859–15869, 2023. 1, 2
- [18] Pamela J LaMontagne, Tammie LS Benzinger, John C Morris, Sarah Keefe, Russ Hornbeck, Chengjie Xiong, Elizabeth Grant, Jason Hassenstab, Krista Moulder, Andrei G Vlassenko, et al. Oasis-3: longitudinal neuroimaging, clinical, and cognitive dataset for normal aging and alzheimer disease. *medrxiv*, pages 2019–12, 2019. 5

[19] Bennett Landman, Zhoubing Xu, J Igelsias, Martin Styner, Thomas Langerak, and Arno Klein. Miccai multi-atlas labeling beyond the cranial vault–workshop and challenge. In *Proc. MICCAI Multi-Atlas Labeling Beyond Cranial Vault—Workshop Challenge*, page 12, 2015. 6

[20] Haofeng Li, Yiming Ouyang, and Xiang Wan. Self-supervised alignment learning for medical image segmentation. In *2024 IEEE International Symposium on Biomedical Imaging (ISBI)*, pages 1–5. IEEE, 2024. 2

[21] Chengzhi Mao, Lingyu Zhang, Abhishek Vaibhav Joshi, Junfeng Yang, Hao Wang, and Carl Vondrick. Robust perception through equivariance. In *International Conference on Machine Learning*, pages 23852–23870. PMLR, 2023. 3

[22] Susanne G Mueller, Michael W Weiner, Leon J Thal, Ronald C Petersen, Clifford Jack, William Jagust, John Q Trojanowski, Arthur W Toga, and Laurel Beckett. The alzheimer’s disease neuroimaging initiative. *Neuroimaging Clinics of North America*, 15(4):869, 2005. 5, 6

[23] Aaron van den Oord, Yazhe Li, and Oriol Vinyals. Representation learning with contrastive predictive coding. *arXiv preprint arXiv:1807.03748*, 2018. 1, 3

[24] Ignacio Rocco, Mircea Cimpoi, Relja Arandjelović, Akihiko Torii, Tomas Pajdla, and Josef Sivic. Neighbourhood consensus networks. *Advances in neural information processing systems*, 31, 2018. 4

[25] Peter J Rousseeuw. Silhouettes: a graphical aid to the interpretation and validation of cluster analysis. *Journal of computational and applied mathematics*, 20:53–65, 1987. 8

[26] Ainkaran Santhirasekaram, Mathias Winkler, Andrea Rockall, and Ben Glocker. A geometric approach to robust medical image segmentation. *Medical Image Analysis*, 97:103260, 2024. 2

[27] Paul-Edouard Sarlin, Daniel DeTone, Tomasz Malisiewicz, and Andrew Rabinovich. Superglue: Learning feature matching with graph neural networks. In *Proceedings of the IEEE/CVF conference on computer vision and pattern recognition*, pages 4938–4947, 2020. 4

[28] William F Sharpe. Mutual fund performance. *The Journal of business*, 39(1):119–138, 1966. 4

[29] Amber L Simpson, Michela Antonelli, Spyridon Bakas, Michel Bilello, Keyvan Farahani, Bram Van Ginneken, Annette Kopp-Schneider, Bennett A Landman, Geert Litjens, Bjoern Menze, et al. A large annotated medical image dataset for the development and evaluation of segmentation algorithms. *arXiv preprint arXiv:1902.09063*, 2019. 1, 6

[30] Richard Sinkhorn. A relationship between arbitrary positive matrices and doubly stochastic matrices. *The annals of mathematical statistics*, 35(2):876–879, 1964. 4

[31] Jiaming Sun, Zehong Shen, Yuang Wang, Hujun Bao, and Xiaowei Zhou. Loftr: Detector-free local feature matching with transformers. In *Proceedings of the IEEE/CVF conference on computer vision and pattern recognition*, pages 8922–8931, 2021. 4

[32] Aiham Taleb, Winfried Loetzsch, Noel Danz, Julius Severin, Thomas Gaertner, Benjamin Bergner, and Christoph Lippert. 3d self-supervised methods for medical imaging. *Advances in neural information processing systems*, 33:18158–18172, 2020. 6

[33] Yucheng Tang, Dong Yang, Wenqi Li, Holger R Roth, Bennett Landman, Daguang Xu, Vishwesh Nath, and Ali Hatamizadeh. Self-supervised pre-training of swin transformers for 3d medical image analysis. In *Proceedings of the IEEE/CVF conference on computer vision and pattern recognition*, pages 20730–20740, 2022. 2

[34] Xing Tao, Yuexiang Li, Wenhui Zhou, Kai Ma, and Yefeng Zheng. Revisiting rubik’s cube: Self-supervised learning with volume-wise transformation for 3d medical image segmentation. In *Medical Image Computing and Computer Assisted Intervention–MICCAI 2020: 23rd International Conference, Lima, Peru, October 4–8, 2020, Proceedings, Part IV 23*, pages 238–248. Springer, 2020. 2, 6

[35] MTCAJ Thomas and A Thomas Joy. *Elements of information theory*. Wiley-Interscience, 2006. 4

[36] Yao-Hung Hubert Tsai, Yue Wu, Ruslan Salakhutdinov, and Louis-Philippe Morency. Self-supervised learning from a multi-view perspective. *arXiv preprint arXiv:2006.05576*, 2020. 3

[37] Chengyao Wang, Li Jiang, Xiaoyang Wu, Zhiyao Tian, Bo-hao Peng, Hengshuang Zhao, and Jiaya Jia. Groupcontrast: Semantic-aware self-supervised representation learning for 3d understanding. In *Proceedings of the IEEE/CVF Conference on Computer Vision and Pattern Recognition*, pages 4917–4928, 2024. 3

[38] Xinlong Wang, Rufeng Zhang, Chunhua Shen, Tao Kong, and Lei Li. Dense contrastive learning for self-supervised visual pre-training. In *Proceedings of the IEEE/CVF conference on computer vision and pattern recognition*, pages 3024–3033, 2021. 3

[39] Yiqing Wang, Zihan Li, Jieru Mei, Zihao Wei, Li Liu, Chen Wang, Shengtian Sang, Alan L Yuille, Cihang Xie, and Yuyin Zhou. Swinmm: masked multi-view with swin transformers for 3d medical image segmentation. In *International Conference on Medical Image Computing and Computer-Assisted Intervention*, pages 486–496. Springer, 2023. 1, 2, 3, 5, 6, 7, 8

[40] Linshan Wu, Jiaxin Zhuang, and Hao Chen. Voco: A simple-yet-effective volume contrastive learning framework for 3d medical image analysis. In *Proceedings of the IEEE/CVF Conference on Computer Vision and Pattern Recognition*, pages 22873–22882, 2024. 1, 2, 3, 5, 6, 7, 8

[41] Zhenda Xie, Zheng Zhang, Yue Cao, Yutong Lin, Jianmin Bao, Zhiliang Yao, Qi Dai, and Han Hu. Simmim: A simple framework for masked image modeling. In *Proceedings of the IEEE/CVF conference on computer vision and pattern recognition*, pages 9653–9663, 2022. 6

[42] Zhangsihao Yang, Mengwei Ren, Kaize Ding, Guido Gerig, and Yalin Wang. Keypoint-augmented self-supervised learning for medical image segmentation with limited annotation. *Advances in Neural Information Processing Systems*, 36, 2024. 2

[43] Xin Yi, Ekta Walia, and Paul Babyn. Generative adversarial network in medical imaging: A review. *Medical image analysis*, 58:101552, 2019. 7

[44] Chuyan Zhang, Hao Zheng, and Yun Gu. Dive into the details of self-supervised learning for medical image analysis. *Medical Image Analysis*, 89:102879, 2023. 6

- [45] Kang Zhang, Xiaohong Liu, Jun Shen, Zhihuan Li, Ye Sang, Xingwang Wu, Yunfei Zha, Wenhua Liang, Chengdi Wang, Ke Wang, et al. Clinically applicable ai system for accurate diagnosis, quantitative measurements, and prognosis of covid-19 pneumonia using computed tomography. *Cell*, 181(6):1423–1433, 2020. [6](#)
- [46] Zhemin Zhang and Xun Gong. Positional label for self-supervised vision transformer. In *Proceedings of the AAAI Conference on Artificial Intelligence*, pages 3516–3524, 2023. [6](#)
- [47] Hong-Yu Zhou, Chixiang Lu, Sibei Yang, Xiaoguang Han, and Yizhou Yu. Preservational learning improves self-supervised medical image models by reconstructing diverse contexts. In *Proceedings of the IEEE/CVF International Conference on Computer Vision*, pages 3499–3509, 2021. [6](#)
- [48] Hong-Yu Zhou, Chixiang Lu, Chaoqi Chen, Sibei Yang, and Yizhou Yu. Pcrlv2: A unified visual information preservation framework for self-supervised pre-training in medical image analysis. *arXiv preprint arXiv:2301.00772*, 2023. [2](#), [3](#), [6](#), [7](#)
- [49] Zongwei Zhou, Vatsal Sodha, Jiaxuan Pang, Michael B Gotway, and Jianming Liang. Models genesis. *Medical image analysis*, 67:101840, 2021. [6](#)
- [50] Jiaxin Zhuang, Linshan Wu, Qiong Wang, Varut Vardhanabhuti, Lin Luo, and Hao Chen. Mim: Mask in mask self-supervised pre-training for 3d medical image analysis. *arXiv preprint arXiv:2404.15580*, 2024. [2](#)
- [51] Jia-Xin Zhuang, Luyang Luo, and Hao Chen. Advancing volumetric medical image segmentation via global-local masked autoencoder. *arXiv preprint arXiv:2306.08913*, 2023. [2](#), [6](#)